Optics Letters

# Broadband second-harmonic generation in an angle-cut lithium niobate-on-insulator waveguide by a temperature gradient

Yongzhi Tang,[1] Tingting Ding,[2] Chuanyi Lu,[1] Jing Qiu,[1] Yuting Zhang,[1] Yiwen Huang,[1] Shijie Liu,[1] Yuanlin Zheng,[1,3,5] and Xianfeng Chen[1,3,4,*]

[1]State Key Laboratory of Advanced Optical Communication Systems and Networks, School of Physics and Astronomy, Shanghai Jiao Tong University, Shanghai 200240, China
[2]School of Electronic and Electrical Engineering, Shanghai University of Engineering Science, Shanghai 201620, China
[3]Shanghai Research Center for Quantum Sciences, Shanghai 201315, China
[4]Collaborative Innovation Center of Light Manipulations and Applications, Shandong Normal University, Jinan 250358, China
[5]e-mail: ylzheng@sjtu.edu.cn
*Corresponding author: xfchen@sjtu.edu.cn

Received 21 November 2022; revised 8 December 2022; accepted 17 January 2023; posted 19 January 2023; published 16 February 2023

**Frequency conversion via nonlinear wave mixing is an important technology to broaden the spectral range of lasers, propelling their applications in optical communication, spectroscopy, signal processing, and quantum information. Many applications require not only a high conversion efficiency but also a broad phase matching bandwidth. Here, we demonstrate broadband birefringence phase matching (BPM) second-harmonic generation (SHG) in angle-cut lithium niobate-on-insulator (LNOI) ridge waveguides based on a temperature gradient scheme. The bandwidth and shift of the phase matching spectrum can be effectively tuned by controlling the temperature gradient of the waveguide. Broadband SHG of a telecom C-band femtosecond laser is also demonstrated. The approach may open a new avenue for tunable broadband nonlinear frequency conversion in various integrated photonics platforms.** 

https://doi.org/10.1364/OL.481649

With the advent of ultrashort pulse lasers, the construction of quantum communication networks and the development of integrated optical chip technology, the demand for miniaturized and integrated broadband frequency conversion devices has increased [1,2]. To date, these devices have played an irreplaceable role in many fields. For instance, broadband frequency conversion helps to achieve all-optical wavelength conversion and build a multi-channel wavelength division multiplexer (WDM) to meet the need of large-capacity optical communication [3,4]. In addition, it can improve the generation efficiency of entangled photon pairs in quantum communication [5–7]. Owing to the inefficiency and high noise of infrared detectors, broadband frequency conversion provides an alternative method to upconvert infrared light to visible for detection [8]. In recent years, many schemes have been proposed to achieve broadband phase matching. For nonlinear optical crystals, there are spectral angular dispersion, chirped matching, adiabatic phase matching [9,10], multiple crystal cascade [11], and noncritical phase matching [12] schemes. For micro- or nano-scale optical devices, there are step chirped polarization [13–15], metamaterials [16,17], and group velocity matching (GVM) [18] schemes, and schemes that involve combining periodic polarization and dispersion engineering [19–22] to achieve broadband frequency conversion. Compared with these schemes, which have a common problem that the matching wavelength cannot be flexibly adjusted over a wide range, the temperature gradient scheme has significant advantages in thermo-optic tunability and flexibility. Our scheme can realize broadband second-harmonic generation (SHG) at different wavelengths and with tunable bandwidths just by controlling the temperature gradient along the waveguide. The chirped quasi-phase matching method is commonly used to operate over a wide range, and can use the largest nonlinear coefficient $d_{33}$ via type-0 configuration [23,24]. However, the thermo-optic tunability is limited and the bandwidth is fixed. The temperature gradient scheme avoids these problems and its conversion efficiency is also satisfying for ultrashort pulses. Moreover, it can be applied to other materials in which periodic poling is challenging.

In recent years, integrated optical chips have played a more and more important role. The emergence of lithium niobate-on-insulator (LNOI) has triggered a revolution in the field of integrated optics [25,26]. Compared with other nonlinear materials, such as indium phosphide, silicon nitride, and aluminum nitride [27–30], LNOI holds greater potential in achieving multifunctional optical chips. Lithium niobate, also known as the “silicon of photonics,” has excellent optical properties, such as a wide transparent window, high refractive index, strong second-order nonlinearity, large electro-optic coefficient, and remarkable thermo-optic effects. The LNOI platform enables the development of optical devices toward dense integration, and it confines light in submicrometer-scale structures, greatly enhancing light–matter interaction [31,32].

Here, we demonstrate a temperature gradient scheme to realize broadband birefringence phase matching (BPM) SHG in

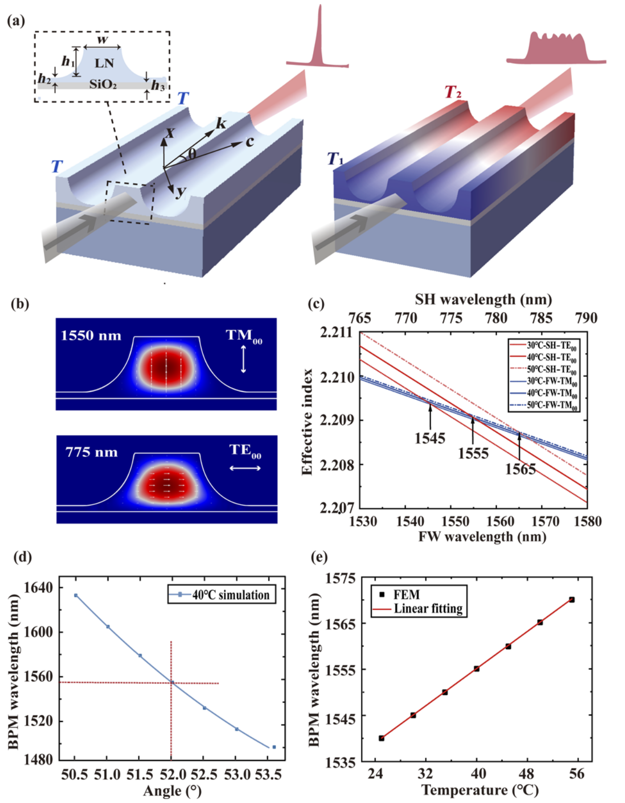


**Fig. 1.** (a) Angle-cut ridge waveguide structure with temperature gradient. (b) Mode profiles for FW and SH waves in ridge waveguide. (c) Simulated effective refractive indices of $TE_{00}$ and $TE_{00}$ modes at 30°C, 40°C, and 50°C as a function of wavelength. (d) Numerically calculated relationship between BPM wavelength and defined cutting angle. (e) Calculated temperature dependence of BPM wavelength. In (c)–(e), simulations take into account the temperature and wavelength dependence of the material refractive indices.

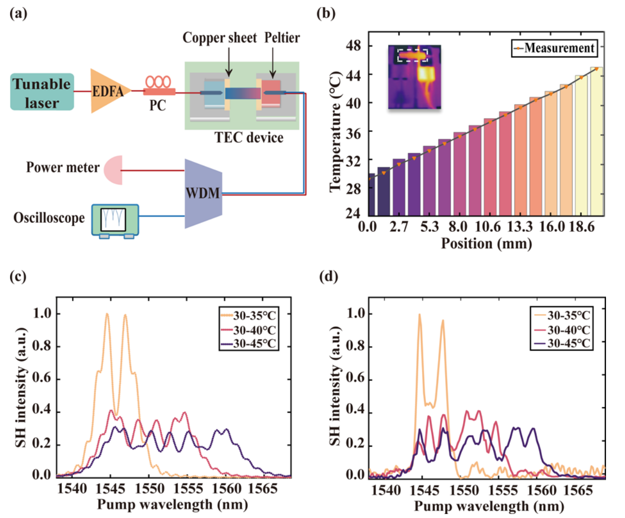


**Fig. 2.** (a) Experiment setup. (b) Measured temperature distribution along waveguide as a function of position. Inset: infrared thermal image of sample. (c) Simulated broadband SH curves at different temperature gradients. (d) Measured broadening of BPM spectra at different temperature gradients.

angle-cut ridge waveguides on a LNOI platform. The type-I BPM scheme has better thermal tunability than the type-0 quasi-phase matching (QPM) method [33,34]. The BPM spectrum redshifts at a value of 1.01 nm/K with increasing temperature. Thus, at a temperature gradient of 30–45°C, the full width at half maximum (FWHM) of the spectrum reaches 15 nm. Broadband nonlinear frequency conversion based on a temperature gradient may have application prospects in ultrafast optics, spectroscopy, optical communication, and quantum optics.

The temperature gradient waveguide is shown, schematically, in Fig. 1(a). The waveguide is placed on two thermoelectric cooler temperature controllers to create a stable temperature gradient. Angle cutting means that there is an angle $\theta$ between the waveguide propagation direction ($k$) and the optical axis ($c$). The BPM condition is achieved when $\theta$ is equal to the phase matching angle at a given temperature. The sample we adopted is a 20-mm-long 52°-cut LNOI ridge waveguide, fabricated by diamond dicing from x-cut LNOI wafer [35,36]. The LNOI wafer consists of 10-µm-thick lithium niobate (LN) and a 2-µm-thick silicon dioxide layer on a 500-µm-thick silicon handle. The shape and dimensions of the waveguide are shown in the inset of Fig. 1(a). The parameters are $h_1 = 9$ µm, $h_2 = 1$ µm, $h_3 = 2$ µm, and $w = 10$ µm. Figure 1(b) shows the simulated mode distribution of $TE_{00}$ at 1550 nm and $TE_{00}$ at 775 nm, and the calculated overlap factor of the spatial mode between the fundamental wave (FW) and its second-harmonic (SH) mode is 0.984.

For LN, the refractive index of o-polarized light changes very slowly with temperature, while the refractive index of e-polarized light varies significantly with temperature. It exhibits strong thermal and optical birefringence under type-I configuration:

$$\left|\frac{dn_e}{dT} - \frac{dn_o}{dT}\right| \approx 4 \times 10^{-5}\ \mathrm{K}^{-1}$$

[33]. Figure 1(c) shows the calculated effective refractive indices of the FW and SH in the 52°-cut LNOI ridge waveguide at 30, 40, and 50°C. The three intersection points indicate that the BPM wavelengths are 1545 nm, 1555 nm, and 1565 nm, respectively. The BPM wavelength redshifts as the temperature increases. Figure 1(d) shows the curve of BPM wavelength as a function of the cutting angle of the waveguide at a temperature of 40°C. It can be seen that the BPM wavelength has a strong dependence on the cutting angle. As shown in Fig. 1(e), it approximately meets the rule that the slope of BPM wavelength of the waveguide with temperature change is 1.01 nm/K.

The experimental setup is shown in Fig. 2(a). The pump source is a tunable external-cavity semiconductor laser (1520–1600 nm), whose power is amplified by an erbium-doped fiber amplifier (EDFA). The polarization state of the incident light is controlled to TM mode by a polarization controller (PC) and the light is coupled into and out of the waveguide via end coupling through single-mode tapered lens fibers. The waveguide is placed on two thermoelectric coolers (TECs) controlled by a computer to form a stable temperature gradient. The output pump light and the generated SH are separated by a 780/1550 nm WDM. Then they are monitored by an oscilloscope and a power meter.

In our experiments, the tunable laser output is scanned from 1520 nm to 1570 nm. The SH signal generated from the waveguide is fed into the oscilloscope and converted to the frequency domain. The inset of Fig. 2(b) shows a stable temperature gradient formed in the waveguide recorded by an infrared thermometer. Figure 2(b) also shows the curve of temperature measured by the thermometer at different positions of the waveguide, showing a linear temperature distribution from 30 to 45°C along the waveguide. To investigate the influence of changing temperature gradient on the spectrum broadening of the SH, we theoretically simulate the normalized BPM spectra at temperature gradients of 30–35, 30–40, and 30–45°C; the result is plotted in Fig. 2(c). Experimentally, we use a temperature-controlled device to form corresponding temperature gradients in the waveguide. Figure 2(d) depicts the measured normalized BPM spectra. As the temperature gradient increases, the spectrum gradually broadens. The FWHM of the spectrum approximately broadens by 1 nm with a temperature gradient increase of 1°C, and finally reaches 15 nm at a temperature gradient of 30–45°C; this is consistent with the theoretical simulation result. The measured normalized conversion efficiency of the waveguide is 2.7%/W-cm$^2$ at room temperature [34], and the conversion efficiency decreases with increasing bandwidth, indicating that the trade-off between conversion efficiency and conversion bandwidth still exists. Owing to the limitations of the temperature control device and the length of the waveguide, the larger temperature gradient becomes unstable in our experiment. It is expected that a broader BPM spectrum can be achieved if a number of smaller particles are used to impose a larger stable temperature gradient.

In the theoretical calculation, we use a finite-element method (FEM) to determine the effective refractive indices of modes, considering dispersion according to the temperature-dependent Sellmeier equations of LN and the structure of the waveguide. The infrared thermogram shows that the temperature is uniformly distributed along the waveguide. The temperature distribution $T(z)$ and the wave vector mismatch $\Delta k(T(z), \lambda_{\mathrm{FW}})$ satisfy

$$\begin{cases} T(z) = T(0) + [T(L) - T(0)]\left(\frac{z}{L}\right), \\ \Delta k(T(z), \lambda_{\mathrm{FW}}) = \frac{4\pi}{\lambda_{\mathrm{FW}}}\left[n_{\mathrm{SH}}(T(z), \lambda_{\mathrm{SH}}) - n_{\mathrm{FW}}(T(z), \lambda_{\mathrm{FW}})\right], \end{cases} \tag{1}$$

where $T(0)$ and $T(L)$ are the temperatures at the input and output ends of the waveguide and $n_{\mathrm{SH}}(T(z), \lambda_{\mathrm{SH}}) - n_{\mathrm{FW}}(T(z), \lambda_{\mathrm{FW}})$ represents the difference of refractive index between the fundamental mode of the FW and SH waves in the waveguide. In the case of a lossless SHG process, the slowly varying envelope approximation gives the coupled mode equations:

$$\begin{cases} \frac{dA_{\mathrm{FW}}}{dz} = -i\kappa A_{\mathrm{SH}} A_{\mathrm{FW}}^{*} \exp\left[-i\Delta k(T(z), \lambda_{\mathrm{FW}})z\right], \\ \frac{dA_{\mathrm{SH}}}{dz} = -i\kappa A_{\mathrm{FW}}^{2} \exp\left[i\Delta k(T(z), \lambda_{\mathrm{FW}})z\right], \end{cases} \tag{2}$$

where $A$ is the field amplitude and $\kappa$ is the nonlinear coupling coefficient. The coupled wave equations are numerically solved and the normalized spectrum of SH intensity, varying with temperature gradients, is obtained, as shown in Figs. 2(c) and 3.

In addition, we simulate the normalized BPM spectrum under different temperature differences by setting the temperature of the input end to 30°C and varying the temperature of the output end. As shown in Fig. 3(a), when the temperature difference $\Delta T = 0$°C or very small, the phase matching condition can only be satisfied at a single wavelength. As $\Delta T$ gradually increases, phase matching can occur at a number of wavelengths simultaneously and eventually appear as a broadband BPM spectrum. We adjust the temperature gradient to shift the broadband BPM spectrum. We set the temperature gradient to be 20–30, 30–40, and 40–50°C, and the normalized SH curve measured is shown in Fig. 3(b). The temperature difference is kept constant at 10°C. With the increase in temperature, the wideband BPM spectrum gradually redshifts, greatly increasing the tunability of our temperature gradient scheme. Although the BPM conversion efficiency is lower than that of QPM, the overall conversion efficiency would still be comparable for ultrashort pulses.

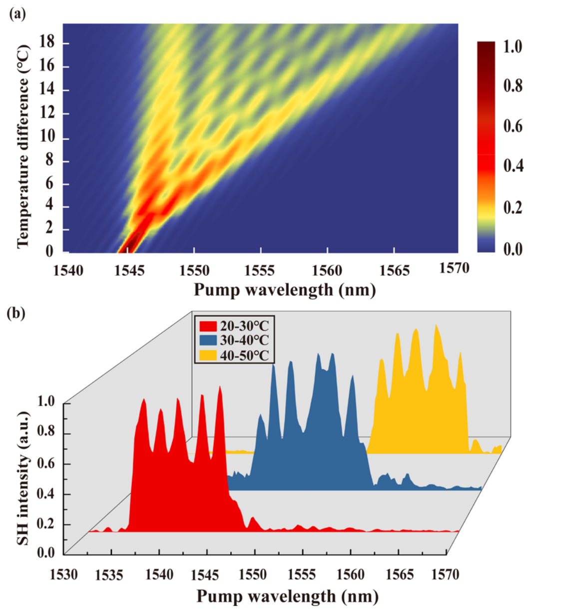


**Fig. 3.** (a) Simulated BPM spectra at different temperature gradients. (b) Measured broadband BPM spectra at different temperature gradients.

Finally, we use a fiber mode locked laser with a center wavelength of 1560 nm (duration 500 fs, repetition rate 60 MHz) to achieve broadband SHG from 1540 nm to 1570 nm in the waveguide. An optical spectrum analyzer (OSA) is used to measure the SH spectrum generated at the output end of the waveguide. Figure 4(a) shows the spectrum of the femtosecond laser.

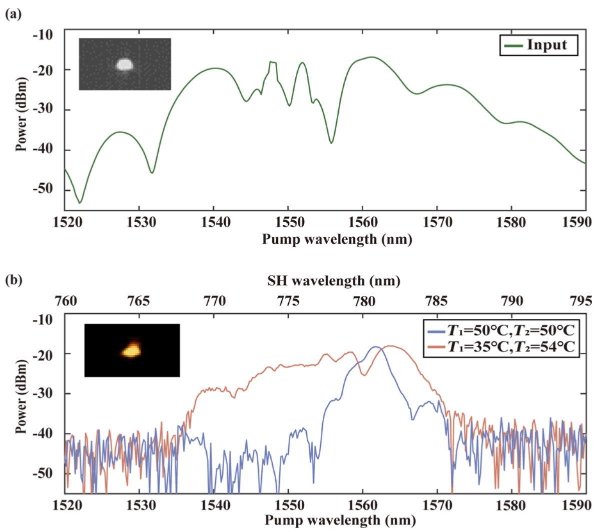


**Fig. 4.** (a) Measured FW curve of femtosecond laser. (b) Measured SH curve of ridge waveguide. Insets: CCD images of pump and SHG fundamental mode profiles at output waveguide facet.

Figure 4(b) shows two SH spectra; one is produced under the condition that the temperature at both ends is 50°C and the other covers a wavelength range from 1538 nm to 1570 nm and is generated by using a temperature gradient of 35–54°C. The insets of Fig. 4 show the experimentally recorded mode profiles of the pump and SH. They are both fundamental modes and therefore have a larger spatial mode overlapping factor [37]. As a result, it can be seen that the temperature gradient scheme combined with an ultrashort pulse laser can also achieve broadband frequency doubling.

In conclusion, we propose and demonstrate a scheme for implementing broadband SHG in integrated waveguides by applying a temperature gradient. The experiment adopts a 52°-cut LNOI ridge waveguide, avoiding a complex periodic polarization process, and uses the BPM method, which has flexible thermo-optic tunability. Under the condition of continuous light input, temperature differences of 5, 10, and 15°C are formed at both ends of the waveguide through the temperature control device, thereby generating broadband frequency doubling with a bandwidth from 5 nm to 15 nm in the telecommunication band. When the temperature difference between the two ends of the waveguide is fixed to 10°C and the overall temperature of the waveguide is increased, the broadened SH curve can be moved to the long wavelength at a speed of 1.01 nm/K, and has great flexibility and tunability. Finally, broadband frequency doubling from 1538 nm to 1570 nm is demonstrated using a femtosecond pulsed laser. In fact, the scheme we propose is not only suitable for broadband frequency doubling in LN waveguides, but can also be extended to other birefringent materials, as well as other second-order nonlinear effects, such as sum or difference frequency generation. This holds potential in applications in the fields of integrated broadband nonlinear frequency conversion and ultrashort pulse compression.

**Funding.** National Natural Science Foundation of China (12074252, 12192252, 62005159, 62022058); National Key Research and Development Program of China (2017YFA0303701, 2018YFA0306301); Shanghai Municipal Science and Technology Major Project (2019SHZDZX01-ZX06); Shanghai Rising-Star Program (20QA1405400); Shanghai Jiao Tong University (501100004921) (21X010200828); Yangyang Development Fund.

**Disclosures.** The authors declare no conflicts of interest.

**Data availability.** Data underlying the results presented in this paper are not publicly available at this time but may be obtained from the authors upon reasonable request.

## REFERENCES

1. D. Zhu, L. Shao, M. Yu, R. Cheng, B. Desiatov, C. J. Xin, Y. Hu, J. Holzgrafe, S. Ghosh, A. Shams-Ansari, E. Puma, N. Sinclair, C. Reimer, M. Zhang, and M. Lončar, Adv. Opt. Photonics **13**, 242 (2021).
2. Y. Zheng and X. Chen, Adv. Phys.: X **6**, 1889402 (2021).
3. P. Fisher, M. Villa, F. Lenzini, and M. Lobino, Phys. Rev. Appl. **13**, 024017 (2020).
4. D. Kong, Y. Liu, Z. Ren, Y. Jung, C. Kim, Y. Chen, N. V. Wheeler, M. N. Petrovich, M. Pu, K. Yvind, M. Galili, L. K. Oxenløwe, D. J. Richardson, and H. Hu, Nat. Commun. **13**, 4139 (2022).
5. Y. Huang, J. Feng, Y. Li, Z. Qi, C. Lu, Y. Zheng, and X. Chen, Phys. Rev. Appl. **17**, 054002 (2022).
6. P. Fisher, R. Cernansky, B. Haylock, and M. Lobino, Phys. Rev. Lett. **127**, 023602 (2021).
7. U. A. Javid, J. Ling, J. Staffa, M. Li, Y. He, and Q. Lin, Phys. Rev. Lett. **127**, 183601 (2021).
8. T.-T. Yeh, H. Shirai, C.-M. Tu, T. Fuji, T. Kobayashi, and C.-W. Luo, Sci. Rep. **7**, 40492 (2017).
9. E. Dimova, V. Steflekova, S. Karatodorov, and E. Kyoseva, J. Phys.: Conf. Ser. **992**, 012007 (2018).
10. E. Rozenberg and A. Arie, Opt. Lett. **44**, 3358 (2019).
11. X. Feng, J. Shi, P. Liu, and Z. Zhang, Opt. Express **28**, 14310 (2020).
12. P. S. Kuo, Opt. Lett. **47**, 54 (2022).
13. X. Wu, L. Zhang, Z. Hao, R. Zhang, R. Ma, F. Bo, G. Zhang, and J. Xu, Opt. Lett. **47**, 1574 (2022).
14. H. Chen, H. Huang, J. Cheng, X. Zhang, X. Feng, X. Cheng, L. Ma, K. Gu, W. Liang, and W. Lin, Opt. Express **30**, 32110 (2022).
15. L. Zhang, Z. Hao, Q. Luo, A. Gao, R. Zhang, C. Yang, F. Gao, F. Bo, G. Zhang, and J. Xu, Opt. Lett. **45**, 3353 (2020).
16. C. Wang, Z. Li, M.-H. Kim, X. Xiong, X.-F. Ren, G.-C. Guo, N. Yu, and M. Loncar, Nat. Commun. **8**, 2098 (2017).
17. J. Li, G. Hu, L. Shi, N. He, D. Li, Q. Shang, Q. Zhang, H. Fu, L. Zhou, W. Xiong, J. Guan, J. Wang, S. He, and L. Chen, Nat. Commun. **12**, 6425 (2021).
18. P. Kumar, M. Younesi, S. Saravi, F. Setzpfandt, and T. Pertsch, Front. Photon. **3**, 951949 (2022).
19. L. Ge, Y. Chen, H. Jiang, G. Li, B. Zhu, Y. Liu, and X. Chen, Photonics Res. **6**, 954 (2018).
20. M. Jankowski, C. Langrock, B. Desiatov, A. Marandi, C. Wang, M. Zhang, C. R. Phillips, M. Lončar, and M. M. Fejer, Optica **7**, 40 (2020).
21. N. Singh, M. Raval, A. Ruocco, and M. R. Watts, Light: Sci. Appl. **9**, 17 (2020).
22. E. Nitiss, B. Zabelich, O. Yakar, J. Liu, R. N. Wang, T. J. Kippenberg, and C.-S. Brès, Photonics Res. **8**, 1475 (2020).
23. J. Chen, C. Tang, Z. Ma, Z. Li, Y. M. Sua, and Y. Huang, Opt. Lett. **45**, 3789 (2020).
24. Z. Hao, L. Zhang, W. Mao, A. Gao, X. Gao, F. Gao, F. Bo, G. Zhang, and J. Xu, Photonics Res. **8**, 311 (2020).
25. Y. Jia, L. Wang, and F. Chen, Appl. Phys. Rev. **8**, 011307 (2021).
26. A. Honardoost, K. E. A. Abdelsalam, and S. Fathpour, Laser Photonics Rev. **14**, 2000088 (2020).
27. D. T. H. Tan, D. K. T. Ng, J. W. Choi, E. Sahin, B. U. Sohn, G. F. R. Chen, P. Xing, H. Gao, and Y. Cao., Adv. Phys.: X **6**, 1905544 (2021).
28. J. Liu, G. Huang, R. N. Wang, J. He, A. S. Raja, T. Liu, N. J. Engelsen, and T. J. Kippenberg, Nat. Commun. **12**, 2236 (2021).
29. N. Li, C. P. Ho, S. Zhu, Y. H. Fu, Y. Zhu, and L. Y. T. Lee, Nanophotonics **10**, 2347 (2021).
30. G. Terrasanta, T. Sommer, M. Müller, M. Althammer, R. Gross, and M. Poot, Opt. Express **30**, 8537 (2022).
31. J. Lin, F. Bo, Y. Cheng, and J. Xu, Photonics Res. **8**, 1910 (2020).
32. Y. Qi and Y. Li, Nanophotonics **9**, 1287 (2020).
33. R. Luo, Y. He, H. Liang, M. Li, and Q. Lin, Optica **5**, 1006 (2018).
34. C. Lu, Y. Zhang, J. Qiu, Y. Tang, T. Ding, S. Liu, Y. Zheng, and X. Chen, Opt. Lett. **47**, 1081 (2022).
35. Q. Zhu, X. Long, Y. Wang, X. Shen, H. Guo, L. Fu, and C. Liu, Opt. Eng. **58**, 1 (2019).
36. J. You, X. Huang, S. Lin, L. Zhang, L. Fu, Q. Yue, S. Lin, and C. Liu, Appl. Opt. **60**, 9146 (2021).
37. J. Lu, J. B. Surya, X. Liu, A. W. Bruch, Z. Gong, Y. Xu, and H. X. Tang, Optica **6**, 1455 (2019).